

A “lighthouse” laser-driven staged proton accelerator allowing for ultrafast angular and spectral control

V. Horný,^{1,2,3,4,*} K. Burdonov,^{1,5} A. Fazzini,¹ V. Lelasseux,^{1,4} P. Antici,⁶ S.N. Chen,⁴ A. Ciardi,⁵ X. Davoine,^{2,3} E. d’Humières,⁷ L. Gremillet,^{2,3} L. Lecherbourg,^{2,3} F. Mathieu,¹ D. Papadopoulos,¹ W. Yao,^{1,5} and J. Fuchs^{1,†}

¹LULI - CNRS, CEA, Sorbonne Université, Ecole Polytechnique,
Institut Polytechnique de Paris - F-91128 Palaiseau cedex, France

²CEA, DAM, DIF, 91297 Arpajon, France

³Université Paris-Saclay, CEA, LMCE, 91680 Bruyères-le-Châtel, France

⁴ELI NP, “Horia Hulubei” National Institute for Physics and Nuclear Engineering,
30 Reactorului Street, RO-077125, Bucharest-Magurele, Romania

⁵Sorbonne Université, Observatoire de Paris, Université PSL, CNRS, LERMA, F-75005, Paris, France

⁶INRS-EMT, 1650, boulevard Lionel-Boulet, J3X 1S2, Varennes (Québec), Canada

⁷Université de Bordeaux, CNRS, CEA, CELIA (Centre Lasers Intenses et Applications), UMR 5107, Talence, France

(Dated: April 18, 2024)

Compact laser-plasma acceleration of fast ions has made great strides since its discovery over two decades ago, resulting in the current generation of high-energy (≥ 100 MeV) ultracold beams over ultrashort (≤ 1 ps) durations. To unlock broader applications of these beams, we need the ability to tailor the ion energy spectrum. Here, we present a scheme that achieves precisely this by accelerating protons in a “lighthouse” fashion, whereby the highest-energy component of the beam is emitted in a narrow cone, well separated from the lower-energy components. This is made possible by a two-stage interaction in which the rear surface of the target is first set into rapid motion before the main acceleration phase. This approach offers the additional advantages of leveraging a robust sheath acceleration process in standard micron-thick targets and being optically controllable.

The progress made in compact laser-based ion accelerators over the two past decades [1, 2] has opened up promising perspectives across various research areas, including radiography of fast-evolving dense plasmas and electromagnetic fields [3–6], investigations into warm dense matter [7–9] and medical applications [10, 11]. Given continuous advances in the repetition rate of the driving high-power lasers [12], such as the 1 PW BELLA laser running at 1 Hz repetition rate [13], such proton beams will become more widely available and more applications can be expected [14–17].

Yet the feasibility of these applications requires the ions to be accelerated in a robust manner. Among the various schemes explored so far, target normal sheath acceleration (TNSA) [18, 19] has proven to be the most sturdy. Indeed, this process does not necessitate stringent laser conditions such as high temporal intensity contrast [20], and it employs standard micron-thick foils that, in addition, can be rolled as a continuous tape target suitable for high-repetition-rate operation [21]. In detail, it hinges on an ultraintense ($> 10^{18}$ W cm⁻²) laser pulse hitting a solid foil and generating a dense beam of fast electrons. These then propagate through the target to its rear side where they induce a strong electrostatic field. While a small fraction of them can escape into the vacuum [22], the majority are reflected back into the target, where they recirculate [23]. The sheath field, in turn, ionizes the surface atoms and accelerates them along the target normal [24]. Protons from surface contaminants, due to their high charge-to-mass ratio, reach the highest velocities.

Since the discovery of TNSA, however, two major drawbacks have emerged: the broad continuous spectrum of the ion beam and the large angular divergence of its low-energy component [1, 2]. Several strategies have been tested to overcome these issues. One involves conventional devices placed downstream of the beam, in order to refocus and/or energy-select it [25–27]. While effective, this has the disadvantage of inducing major losses in the output ion number, as conventional ion beam optics cannot withstand the high charge associated with laser-driven beams. Alternatively, better-tailored plasma devices have been developed to modify the beam properties, but they either require an additional beam-focusing target positioned after the source target [28], and an additional laser to power it, or rely on engineered targets. These can be droplets [29, 30] or curved solid targets [7, 31, 32], i.e., with more complexity than the flat foils employed in our study.

Here, we demonstrate another method to circumvent the limitations of TNSA, which we term “lighthouse-TNSA”. In this approach, as illustrated by the blue cone in Fig. 1(a), the higher-energy protons, i.e., those naturally generated with a small angular aperture, are angularly shifted away from the lower-energy beam component, which remains accelerated around the target normal [see the green cone in Fig. 1(a)]. As a result, the spectrum of the output protons can be easily adjusted by collecting them along a specific direction. This is achieved by staging the TNSA process in two steps. First, the target rear surface is dynamically tilted by a short (\sim ps) prepulse, before the main pulse arrives and fur-

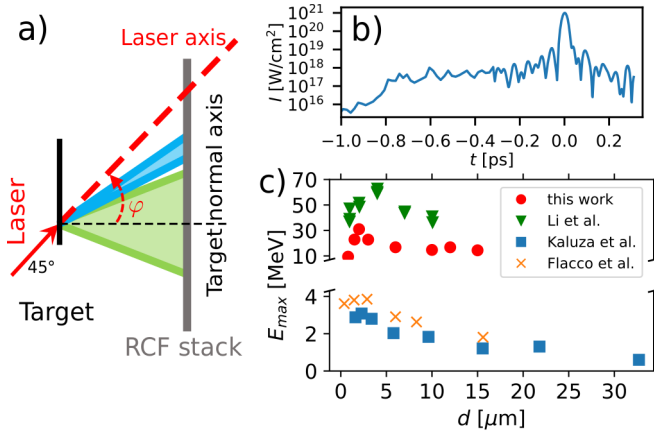


FIG. 1. (a) Experimental setup (see text for details). (b) Temporal intensity profile of the 1 PW Apollon laser pulse as measured within the last ps before the pulse maximum. (c) Cutoff proton energies as measured in this work (red circles) and from literature (green triangles [33], blue squares [34], brown crosses [35]).

ther accelerates the ions from this fast-rotating surface. Such a target conditioning is performed in an all-optical manner by shaping the rising edge of the laser temporal profile [see Fig. 1(b)], so that simple and robust standard, micron-thick targets can still be used.

Previous experiments have shown that an energy-dependent angular shift can be imparted on TNSA ion beams by hydrodynamically deforming the target surface by a long (ns) laser prepulse [33, 36–40]. In this way, however, the high-energy components of the beam remain fully embedded in the broad emission cone of its low-energy component, limiting the ability to collect them separately. By contrast, the scheme we present here has the advantage of steering the target and driving the ions over similar short (ps) time scales, allowing the low-divergence, fastest ions to deviate well away from the slowest ones.

The experiment made use of the 1 PW arm of the Apollon laser system ($\sim 10 \text{ J}$, 24 fs , $2 \times 10^{21} \text{ W cm}^{-2}$) [41]. The setup is sketched in Fig. 1(a). The laser pulse is incident at 45° on thin aluminum targets from which protons are accelerated up to above 30 MeV energies for $2\text{--}3 \mu\text{m}$ thick foils. Due to the very high laser contrast [41], the shock wave generated by the weak ns- and multi-ps-scale prepulses is too slow to reach the target backside before the impact of the main pulse (see details below). Conversely, the relativistically intense ($\geq 10^{18} \text{ W cm}^{-2}$) part of the laser profile arriving within the last ps before the pulse maximum [see Fig. 1(b)] can drive a primary, relatively slow TNSA phase inducing a deformation of the target backside. As will be analyzed below, this deformation will result in the bending of the protons accelerated during the secondary TNSA phase driven by the pulse maximum. Figure 1(c) plots the measured proton cutoff

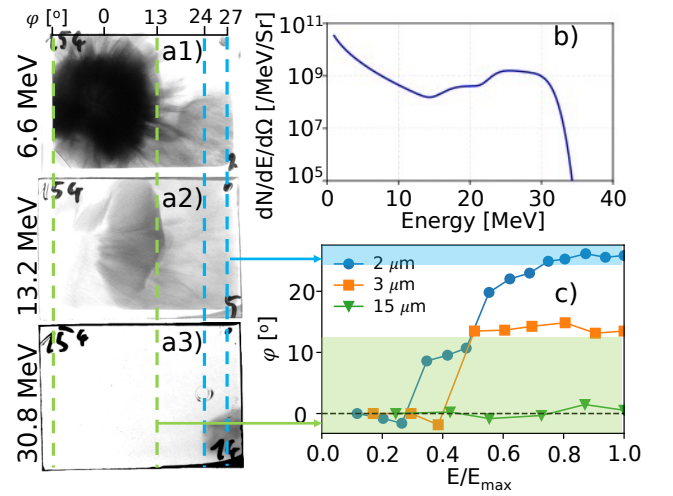


FIG. 2. (a1-a3) Raw RCF data obtained for a $2 \mu\text{m}$ thick Al foil, showing, respectively, protons of low (6.6 MeV), medium (13.2 MeV), and high (30.8 MeV) mean energies, as labelled. (b) Proton energy spectrum within the angular band delimited by the two blue lines in panel (a). (c) Deviation of the emission angle of the protons from the target normal as a function of their energy (normalized to the cutoff energy E_{max}) for three different Al foil thicknesses: $2 \mu\text{m}$ ($E_{\text{max}} = 31 \text{ MeV}$, blue), $3 \mu\text{m}$ ($E_{\text{max}} = 23 \text{ MeV}$, orange) and $15 \mu\text{m}$ ($E_{\text{max}} = 14.4 \text{ MeV}$, green).

energy as a function of the target thickness (d), together with related experimental data from the literature. In our case, a maximum proton energy (i.e. corresponding to the last imprinted radiochromic film) of over 31 MeV was achieved for $d = 2 \mu\text{m}$.

The effect of the proton bending is illustrated in Fig. 2. Figure 2(a) displays the raw data, i.e., some radiochromic films (RCFs) from the stack used to resolve in energy and angle the accelerated proton beam [42], for $d = 2 \mu\text{m}$. The RCFs shown correspond to, respectively, low, medium and high energies (as labeled). Figure 2(b) plots, for the same case, the proton energy spectrum as inferred in the angular range ($24^\circ \lesssim \varphi \lesssim 27^\circ$ from the target normal) indicated by the two dashed blue lines in panel (a). This spectrum shows a pronounced bump in the $\sim 13\text{--}30 \text{ MeV}$ energy range. The lower-energy component remaining in the spectrum likely originates from front-accelerated protons, which are emitted over wider angles [43]. The low-energy, rear-surface accelerated protons are indeed known to be emitted in a low-divergence cone [42]. This component could be suppressed by coating the target front by a thin heavy layer that would stop the front-side protons, but not the fast electrons responsible for rear-side TNSA [44].

Figure 2(c) depicts the deviation of the center of the proton beam measured on each RCF, from the target normal toward the laser beam axis [as also illustrated in Fig. 1(a)]. While all protons accelerated from a $15 \mu\text{m}$

thick foil are emitted along the target normal – a behavior consistent with standard TNSA [18] –, those driven in 2–3 μm thick foils, which reach the highest energies [cf. Fig. 1(c)], exhibit a markedly different behaviour. For these targets, the proton beam exhibits a deviation that is increasing with the kinetic energy. The maximum deviation ($\sim 26^\circ$) is observed for $d = 2 \mu\text{m}$, enabling the highest-energy ($E/E_{\text{max}} \gtrsim 0.8$) beam component [between the dashed blue curves in (a3)] to be fully separated from the low-energy ($E/E_{\text{max}} < 0.5$) component [between the green blue curves in (a3)], centered around the target normal. With the 15 μm thick target, the angular deviation seen with the thinner foil targets is not observed due to a lack of sensitivity to the first TNSA phase which steers the target rear surface. To investigate in detail the TNSA dynamics underlying the “lighthouse” effect observed in Fig. 2, we now turn to particle-in-cell (PIC) simulations, performed with the 2D3V (2D in space, 3D in momentum space) version of the CALDER code [45]. These simulations focus on the plasma evolution within the last picosecond before the temporal peak of the laser pulse. The simulation details are given in the Supplementary Material. Since there is, however, some laser energy prior to this last picosecond, we have separately estimated its impact on the target using the 1D hydrodynamical ESTHER code [46]. This simulation uses the SESAME equation of state 3720 for aluminum [47, 48]. It takes as input the laser rising edge profile ($< 10^{16} \text{ W cm}^{-2}$) that is reported in Ref. [41], here restricted to the $-50 < t < -1$ ps timespan relative to the laser peak [not shown in Fig. 1(b)].

Figure S1 in the Supplemental Material plots the expanding electron and ion density profiles at the end of the ESTHER simulation. We observe that the critical surface ($n_e = n_c$) on the laser-irradiated side is shifted, toward the incident laser, by $\sim 2\text{--}3 \mu\text{m}$ away from the initial target surface. The local density scale-length is measured to be of $(\partial \ln n_e / \partial x)^{-1} \simeq 2 \mu\text{m}$. This extended plasma profile helps to absorb the later, more intense portion of the laser profile. The simulation also reveals a shock wave launched into the target bulk by a strong prepulse, of $\sim 10^{14} \text{ W cm}^{-2}$ intensity and located at $t \simeq -26$ ps [41]. At the end of the ESTHER simulation, i.e. at $t = -1$ ps and when the CALDER simulation starts, the shock has traveled a distance of $\simeq 0.44 \mu\text{m}$, smaller than the thickness of the optimal target used in the experiment ($2 \mu\text{m}$). Therefore, the target backside, as we initiate the CALDER simulation, can be considered unperturbed by the preceding laser prepulse, which is consistent with the observation of a smooth angular pattern for the highest-energy protons, see Fig. 2(a3). This also aligns with the theoretical analysis of Ref. [38], on the basis of which one expects a $10^{14} \text{ W cm}^{-2}$ prepulse to generate a ~ 10 Mbar shock pressure in aluminum. Within the perfect gas approximation, the related shock velocity [49] is of $\sim 22 \mu\text{m ns}^{-1}$, relatively close to the $\sim 18 \mu\text{m ns}^{-1}$ mean shock velocity

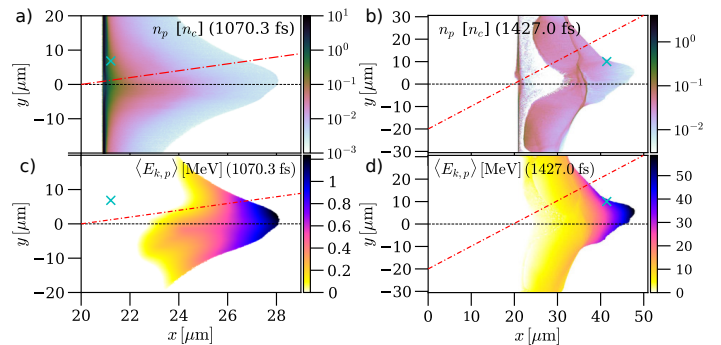


FIG. 3. PIC simulation of staged TNSA in a 1 μm thick foil. Spatial distributions of the (a,b) proton density n_p and (c,d) average proton energy $\langle E_{k,p} \rangle$ at times (a,c) $t = 1073$ fs and (b,d) $t = 1427$ fs. The crosses indicate the position of the sample particle trajectory shown in Fig. 5. The black dashed and red dash-and-dot lines highlight the target normal and laser axis, respectively. Movies showing the evolution of the particle and field quantities are also available in the Supplementary Material [50].

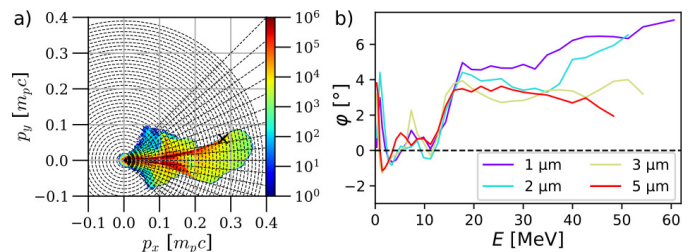


FIG. 4. (a) Proton p_x – p_y phase space from a 1 μm thick target at $t = 1427$ fs. The cross corresponds to the particle tracked in Fig. 2 of the Supplemental Material [50]. The dashed radial lines are separated by 5° . (b) Energy dependence of the average proton deviation from the target normal for several target thicknesses.

predicted by the simulation.

The target density profile as obtained at the end of the ESTHER simulation is used as an input for the CALDER simulation. Figure 3 presents the results of the latter for a 1 μm thick target, in which case the most detailed outputs have been stored. The top and bottom panels show, respectively, the proton particle density and the local mean proton kinetic energy. Figures 3(a) and (c) visualize these profiles just before the main laser pulse hits the target ($t = 1070.3$ fs). A standard TNSA process can be observed. As a result, the protons are preferentially driven in a direction close to the target normal (black dashed line), reaching energies up to 1.2 MeV. Due to the 45° incidence angle of the (upward-propagating) laser wave, the envelope of the proton cloud is somewhat asymmetric relative to the target normal, with the fastest protons traveling slightly off-centre.

An important consequence of this primary TNSA stage is the deformation of the target backside. This affects

the next TNSA stage, triggered by the main pulse, as shown in Fig. 3(b) and (d) just before the accelerated protons exit the simulation box ($t = 1427$ fs). We can see a significant upward bending of the proton front (i.e., towards the laser axis), especially for the fastest protons.

Figure 4(a) takes a closer look at how the protons deviate from the target normal (horizontal axis). It details the proton p_x - p_y phase space at the same time ($t = 1427$ fs) as in Figs. 3(b) and (d). There is a clear trend of angular deflection (by up to $\sim 15^\circ$) towards the laser direction for higher-energy protons. The energy dependence of the average proton deviation angle is plotted in Fig. 4(b) for various target thicknesses. The thinnest targets exhibit the most pronounced deflection. The characteristic shape of the curves, with no deflection at lower energies, a rapid rise to a significant value, and a subsequent plateau or slight increase with energy, is consistent with the experimental observation in Fig. 2(c).

Figure 5 depicts the trajectory of a typical accelerated proton as recorded in the $d = 1 \mu\text{m}$ simulation. The position of this proton is marked with a cross in Figs. 3 and 4(a). Figure 5(a) plots the time evolution of its kinetic energy. The inset details the preacceleration associated with the first TNSA stage, showing that the proton energy reaches ~ 55 keV before the arrival of the main laser pulse ($t = 1070$ fs). In the second stage, the proton gains an energy of ~ 37 MeV within 250 fs. Figure 5(b) plots the time evolution of the longitudinal displacement of the proton from its position ($x_0 = 20.91 \mu\text{m}$) at $t = 951$ fs, when particle tracking started, and its transverse position $y(t)$.

Figure 5(c) plots the evolution of the amplitude of the electric (E_x, E_y) and magnetic (B_z) fields experienced by the sample proton. Noting ω the laser frequency, the electric field components (E_x, E_y) peak at $(3.9, 0.38) m_e c \omega / e$, i.e., $(12.6, 1.25) \text{ TV m}^{-1}$, while the magnetic field attains $B_z = -3.32 m_e c \omega / e$, i.e., 44.4 kT .

Figure 5(d) shows the momentum components of the accelerated proton. Two stages of acceleration are apparent. Within the first slow-acceleration stage, the proton is accelerated mainly along the target normal direction. At $t = 1070$ fs, its longitudinal momentum reaches $p_x \simeq 0.011 m_p c$ while the transverse component is $p_y \simeq 6 \times 10^{-4} m_p c$, corresponding to a deviation $\varphi \simeq 3.2^\circ$. This value represents the standard deviation of TNSA, considering the initial off-axis position of the proton. The second fast-acceleration stage brings about not only a rapid increase in longitudinal momentum but also a significant transverse deviation. The evolution of the proton deviation over time is plotted in Fig. 5(e). The rather large values observed before the main laser pulse are not significant as the effective proton motion is minuscule.

Figure 5(f) addresses the origin of the proton bending. It shows the components of the normalized Lorentz force $\mathbf{f} = \mathbf{F}/e = \mathbf{E} + \mathbf{v} \times \mathbf{B}$, namely, $f_x = E_x$ and $f_y = f_{y,e} + f_{y,m}$ where $f_{y,e} = E_y$ and $f_{y,m} = -v_x B_z$

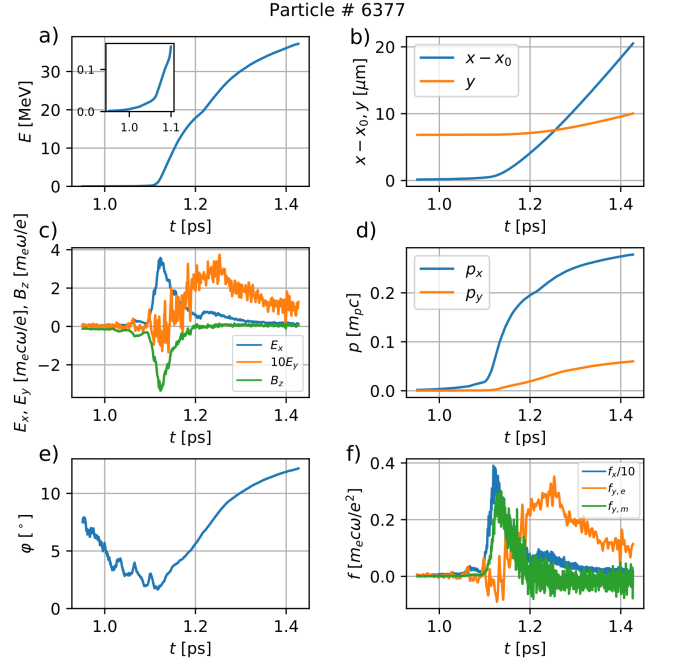


FIG. 5. Typical simulated trajectory of a proton accelerated to high energy. Temporal evolution of (a) kinetic energy, (b) longitudinal and transverse coordinates, (c) experienced electromagnetic field components, (d) momentum components, (e) deviation angle, and (f) Lorentz force components.

represent the electric and magnetic parts of the transverse component of the Lorentz force. As seen from the plot, there is no significant sideways acceleration before the main laser pulse arrives. At this point, the magnetic force ($f_{y,m}$) gives the protons an initial deflection, see Fig. 5(d). However, it is the electric force $f_{y,e}$ that is mainly responsible for deviating the proton towards the laser axis, as can be seen by comparing the areas under the $f_{y,e}$ and $f_{y,m}$ curves.

In summary, we have presented experimental evidence of strong proton bending from the target normal towards the laser axis when micron-thick foils are irradiated with a PW-class femtosecond laser pulse under oblique incidence. The degree of deviation increases with the proton energy to the point where the faster protons can be angularly discriminated from the slower ones. The monotonic energy dependence of the proton deviation holds promise for various applications, especially in medicine [11]. In contrast to previous similar observations, this lighthouse-like emission of fast ions does not result from the convex deformation of the target backside caused by the prepulse/pedestal-induced shock wave [38], because the shock wave is too slow under our conditions. Our combined hydrodynamic and PIC simulations reveal a two-stage TNSA process responsible for the observed bending. The first occurs within the last picosecond prior to the laser peak intensity, leading to a slightly asymmet-

ric expansion of the target backside to \sim MeV energies. The second is triggered by the laser pulse maximum, resulting in both further proton acceleration and bending. Our analysis indicates that the transverse electrostatic field in the expanding plasma is the dominant factor of deviation. We note that very recent simulation work with idealised plasma parameters performed by Pšikal [51] is supporting our analysis.

Importantly, this previously overlooked proton bending process occurs in the TNSA regime with high-power lasers capable of high-repetition-rate operation, potentially leading to extreme proton fluxes as TNSA is known for high particle yields per shot [2]. Furthermore, the parameters of the needed short prepulse could be easily tuned, to a main pulse different than used here, by using a simple and effective fast-prepulse optical shaping technique already established for high-order harmonic generation [52].

The authors acknowledge the national research infrastructure Apollon and the LULI for their technical assistance. This work was supported by funding from the European Research Council (ERC) under the European Unions Horizon 2020 research and innovation program (Grant Agreement No. 787539, Project GENESIS). This work was also supported by the Extreme Light Infrastructure Nuclear Physics (ELI-NP) Phase II, a project co-financed by the Romanian Government and the European Union through the European Regional Development Fund - the Competitiveness Operational Programme (1/07.07.2016, COP, ID 1334); the Romanian Ministry of Research and Innovation: PN23210105 (Phase 2, the Program Nucleu); and the ELI-RO grant Proiectul ELI12/16.10.2020 of the Romanian Government. We acknowledge GENCI-TGCC for granting us access to the supercomputer IRENE under Grants No. A0120507594 and No. A0130512993.

* vojtech.horny@eli-np.ro

† julien.fuchs@polytechnique.edu

- [1] H. Daido, M. Nishiuchi, and A. S. Pirozhkov, Review of laser-driven ion sources and their applications, *Reports on Progress in Physics* **75**, 056401 (2012).
- [2] A. Macchi, M. Borghesi, and M. Passoni, Ion acceleration by superintense laser-plasma interaction, *Reviews of Modern Physics* **85**, 751 (2013).
- [3] N. L. Kugland, D. D. Ryutov, P. Y. Chang, R. P. Drake, G. Fiksel, D. H. Froula, S. H. Glenzer, G. Gregori, M. Grosskopf, M. Koenig, Y. Kuramitsu, C. Kuran, M. C. Levy, E. Liang, J. Meinecke, F. Miniati, T. Morita, A. Pelka, C. Plechaty, R. Presura, A. Ravasio, B. A. Remington, B. Reville, J. S. Ross, Y. Sakawa, A. Spitkovsky, H. Takabe, and H. S. Park, Self-organized electromagnetic field structures in laser-produced counter-streaming plasmas, *Nature Physics* **8**, 809 (2012).
- [4] G. Sarri, A. Macchi, C. A. Cecchetti, S. Kar, T. V. Liseykina, X. H. Yang, M. E. Dieckmann, J. Fuchs, M. Galimberti, L. A. Gizzi, R. Jung, I. Kourakis, J. Osterholz, F. Pegoraro, A. P. L. Robinson, L. Romagnani, O. Willi, and M. Borghesi, Dynamics of Self-Generated, Large Amplitude Magnetic Fields Following High-Intensity Laser Matter Interaction, *Physical Review Letters* **109**, 205002 (2012).
- [5] C. Ruyer, S. Bolaños, B. Albertazzi, S. N. Chen, P. Antici, J. Böker, V. Dervieux, L. Lancia, M. Nakatsutsumi, L. Romagnani, R. Shepherd, M. Swantusch, M. Borghesi, O. Willi, H. Pépin, M. Starodubtsev, M. Grech, C. Riconda, L. Gremillet, and J. Fuchs, Growth of concomitant laser-driven collisionless and resistive electron filamentation instabilities over large spatiotemporal scales, *Nature Physics* **16**, 983 (2020).
- [6] D. B. Schaeffer, A. F. A. Bott, M. Borghesi, K. A. Flippo, W. Fox, J. Fuchs, C. Li, F. H. Séguin, H.-S. Park, P. Tzeferacos, and L. Willingale, Proton imaging of high-energy-density laboratory plasmas, *Reviews of Modern Physics* **95**, 045007 (2023).
- [7] P. Patel, A. Mackinnon, M. Key, T. Cowan, M. Ford, M. Allen, D. Price, H. Ruhl, P. Springer, and R. Stephens, Isochoric heating of solid-density matter with an ultrafast proton beam, *Physical Review Letters* **91**, 125004 (2003).
- [8] A. Mančić, A. Lévy, M. Harmand, M. Nakatsutsumi, P. Antici, P. Audebert, P. Combis, S. Fourmaux, S. Mazevet, O. Peyrusse, V. Recoules, P. Renaudin, J. Robiche, F. Dorchies, and J. Fuchs, Picosecond Short-Range Disorder in Isochorically Heated Aluminum at Solid Density, *Physical Review Letters* **104**, 035002 (2010).
- [9] S. Malko, W. Cayzac, V. Ospina-Bohórquez, K. Bhutwala, M. Bailly-Grandvaux, C. McGuffey, R. Fedosejevs, X. Vaisseau, A. Tauschwitz, J. I. Apiñaniz, D. D. L. Blanco, G. Gatti, M. Huault, J. A. P. Hernandez, S. X. Hu, A. J. White, L. A. Collins, K. Nichols, P. Neumayer, G. Faussurier, J. Vorberger, G. Prestopino, C. Verona, J. J. Santos, D. Batani, F. N. Beg, L. Roso, and L. Volpe, Proton stopping measurements at low velocity in warm dense carbon, *Nature Communications* **13**, 2893 (2022).
- [10] S. V. Bulanov, T. Z. Esirkepov, V. S. Khoroshkov, A. V. Kuznetsov, and F. Pegoraro, Oncological hadrontherapy with laser ion accelerators, *Physics Letters A* **299**, 240 (2002).
- [11] F. Kroll, F.-E. Brack, C. Bernert, S. Bock, E. Bodenstein, K. Brüchner, T. E. Cowan, L. Gaus, R. Gebhardt, U. Helbig, L. Karsch, T. Kluge, S. Kraft, M. Krause, E. Lessmann, U. Masood, S. Meister, J. Metzkes-Ng, A. Nosula, J. Pawelke, J. Pietzsch, T. Püschel, M. Reimold, M. Rehwald, C. Richter, H.-P. Schlenvoigt, U. Schramm, M. E. P. Umlandt, T. Ziegler, K. Zeil, and E. Beyreuther, Tumour irradiation in mice with a laser-accelerated proton beam, *Nature Physics* **18**, 316 (2022).
- [12] C. N. Danson, C. Haefner, J. Bromage, T. Butcher, J.-C. F. Chanteloup, E. A. Chowdhury, A. Galvanauskas, L. A. Gizzi, J. Hein, D. I. Hillier, N. W. Hopps, Y. Kato, E. A. Khazanov, R. Kodama, G. Korn, R. Li, Y. Li, J. Limpert, J. Ma, C. H. Nam, D. Neely, D. Papadopoulos, R. R. Penman, L. Qian, J. J. Rocca, A. A. Shaykin, C. W. Siders, C. Spindloe, S. Szatmári, R. M. G. M. Trines, J. Zhu, P. Zhu, and J. D. Zuegel, Petawatt and exawatt class lasers worldwide, *High Power Laser Science*

- and Engineering **7**, e54 (2019).
- [13] K. Nakamura, H.-S. Mao, A. J. Gonsalves, H. Vincenti, D. E. Mittelberger, J. Daniels, A. Magana, C. Toth, and W. P. Leemans, Diagnostics, control and performance parameters for the BELLA high repetition rate petawatt class laser, *IEEE Journal of Quantum Electronics* **53**, 1 (2017).
- [14] M. Barberio, S. Veltri, M. Scisciò, and P. Antici, Laser-accelerated proton beams as diagnostics for cultural heritage, *Scientific Reports* **7**, 40415 (2017).
- [15] J. C. Fernández, C. W. Barnes, M. J. Mocko, and L. Zavorka, Requirements and sensitivity analysis for temporally- and spatially-resolved thermometry using neutron resonance spectroscopy, *Review of Scientific Instruments* **90**, 094901 (2019).
- [16] M. Passoni, L. Fedeli, and F. Mirani, Superintense laser-driven ion beam analysis, *Scientific Reports* **9**, 9202 (2019).
- [17] V. Horný, S. N. Chen, X. Davoine, L. Gremillet, and J. Fuchs, Quantitative feasibility study of sequential neutron captures using intense lasers, *Physical Review C* **109**, 10.1103/physrevc.109.025802 (2024).
- [18] R. A. Snavely, M. H. Key, S. P. Hatchett, T. E. Cowan, M. Roth, T. W. Phillips, M. A. Stoyer, E. A. Henry, T. C. Sangster, M. S. Singh, S. C. Wilks, A. MacKinnon, A. Ofenberger, D. M. Pennington, K. Yasuike, A. B. Langdon, B. F. Lasinski, J. Johnson, M. D. Perry, and E. M. Campbell, Intense High-Energy Proton Beams from Petawatt-Laser Irradiation of Solids, *Phys. Rev. Lett.* **85**, 2945 (2000).
- [19] S. C. Wilks, A. B. Langdon, T. E. Cowan, M. Roth, M. Singh, S. Hatchett, M. H. Key, D. Pennington, A. MacKinnon, and R. A. Snavely, Energetic proton generation in ultra-intense laser–solid interactions, *Physics of Plasmas* **8**, 542 (2001).
- [20] N. P. Dover, T. Ziegler, S. Assenbaum, C. Bernert, S. Bock, F.-E. Brack, T. E. Cowan, E. J. Ditter, M. Garten, L. Gaus, I. Goethel, G. S. Hicks, H. Kiriya, T. Kluge, J. K. Koga, A. Kon, K. Kondo, S. Kraft, F. Kroll, H. F. Lowe, J. Metzkes-Ng, T. Miyatake, Z. Najmudin, T. Püschel, M. Rehwald, M. Reimold, H. Sakaki, H.-P. Schlenvoigt, K. Shiokawa, M. E. P. Umlandt, U. Schramm, K. Zeil, and M. Nishiuchi, Enhanced ion acceleration from transparency-driven foils demonstrated at two ultraintense laser facilities, *Light: Science & Applications* **12**, 71 (2023).
- [21] N. Dover, M. Nishiuchi, H. Sakaki, K. Kondo, H. Lowe, M. Alkhimova, E. Ditter, O. Ettliger, A. Faenov, M. Hata, G. Hicks, N. Iwata, H. Kiriya, J. Koga, T. Miyahara, Z. Najmudin, T. Pikuz, A. Pirozhkov, A. Sagisaka, U. Schramm, Y. Sentoku, Y. Watanabe, T. Ziegler, K. Zeil, M. Kando, and K. Kondo, Demonstration of repetitive energetic proton generation by ultraintense laser interaction with a tape target, *High Energy Density Physics* **37**, 100847 (2020).
- [22] A. Link, R. R. Freeman, D. W. Schumacher, and L. D. Van Woerkom, Effects of target charging and ion emission on the energy spectrum of emitted electrons, *Physics of Plasmas* **18**, 053107 (2011).
- [23] A. J. Mackinnon, Y. Sentoku, P. K. Patel, D. W. Price, S. Hatchett, M. H. Key, C. Andersen, R. Snavely, and R. R. Freeman, Enhancement of proton acceleration by hot-electron recirculation in thin foils irradiated by ultraintense laser pulses, *Physical Review Letters* **88**, 10.1103/physrevlett.88.215006 (2002).
- [24] P. Mora and T. Grismayer, Rarefaction Acceleration and Kinetic Effects in Thin-Foil Expansion into a Vacuum, *Physical Review Letters* **102**, 145001 (2009).
- [25] J. Teng, Y. Gu, B. Zhu, W. Hong, Z. Zhao, W. Zhou, and L. Cao, Beam collimation and energy spectrum compression of laser-accelerated proton beams using solenoid field and rf cavity, *Nuclear Instruments and Methods in Physics Research Section A: Accelerators, Spectrometers, Detectors and Associated Equipment* **729**, 399–403 (2013).
- [26] S. N. Chen, M. Gauthier, D. P. Higginson, S. Dorard, F. Mangia, R. Riquier, S. Atzeni, J. R. Marquès, and J. Fuchs, Monochromatic short pulse laser produced ion beam using a compact passive magnetic device, *Review of Scientific Instruments* **85**, 043504 (2014).
- [27] F.-E. Brack, F. Kroll, L. Gaus, C. Bernert, E. Beyreuther, T. E. Cowan, L. Karsch, S. Kraft, L. A. Kunz-Schughart, E. Lessmann, J. Metzkes-Ng, L. Obst-Huebl, J. Pawelke, M. Rehwald, H.-P. Schlenvoigt, U. Schramm, M. Sobiella, E. R. Szabó, T. Ziegler, and K. Zeil, Spectral and spatial shaping of laser-driven proton beams using a pulsed high-field magnet beamline, *Scientific Reports* **10**, 9118 (2020).
- [28] T. Toncian, M. Borghesi, J. Fuchs, E. d’Humières, P. Antici, P. Audebert, E. Brambrink, C. A. Cecchetti, A. Pipahl, L. Romagnani, and O. Willi, Ultrafast Laser-Driven Microlens to Focus and Energy-Select Mega-Electron Volt Protons, *Science* **312**, 410 (2006).
- [29] S. Ter-Avetisyan, M. Schnürer, P. V. Nickles, M. Kalashnikov, E. Risse, T. Sokollik, W. Sandner, A. Andreev, and V. Tikhonchuk, Quasimonoenergetic Deuteron Bursts Produced by Ultraintense Laser Pulses, *Physical Review Letters* **96**, 145006 (2006).
- [30] P. Hilz, T. M. Ostermayr, A. Huebl, V. Bagnoud, B. Borm, M. Bussmann, M. Gallei, J. Gebhard, D. Haffa, J. Hartmann, T. Kluge, F. H. Lindner, P. Neumayr, C. G. Schaefer, U. Schramm, P. G. Thirolf, T. F. Rösch, F. Wagner, B. Zielbauer, and J. Schreiber, Isolated proton bunch acceleration by a petawatt laser pulse, *Nature Communications* **9**, 423 (2018).
- [31] T. Bartal, M. E. Foord, C. Bellei, M. H. Key, K. A. Flippo, S. A. Gaillard, D. T. Offermann, P. K. Patel, L. C. Jarrott, D. P. Higginson, M. Roth, A. Otten, D. Kraus, R. B. Stephens, H. S. McLean, E. M. Giraldez, M. S. Wei, D. C. Gautier, and F. N. Beg, Focusing of short-pulse high-intensity laser-accelerated proton beams, *Nature Physics* **8**, 139 (2012).
- [32] S. N. Chen, E. D’Humières, E. Lefebvre, L. Romagnani, T. Toncian, P. Antici, P. Audebert, E. Brambrink, C. A. Cecchetti, T. Kudyakov, A. Pipahl, Y. Sentoku, M. Borghesi, O. Willi, and J. Fuchs, Focusing Dynamics of High-Energy Density, Laser-Driven Ion Beams, *Physical Review Letters* **108**, 055001 (2012).
- [33] A. Li, C. Qin, H. Zhang, S. Li, L. Fan, Q. Wang, T. Xu, N. Wang, L. Yu, Y. Xu, *et al.*, Acceleration of 60 MeV proton beams in the commissioning experiment of SULF-10 PW laser, *High Power Laser Science and Engineering* **10**, e26 (2022).
- [34] M. Kaluza, J. Schreiber, M. I. Santala, G. D. Tsakiris, K. Eidmann, J. Meyer-Ter-Vehn, and K. J. Witte, Influence of the Laser Prepulse on Proton Acceleration in Thin-Foil Experiments, *Physical Review Letters* **93**, 045003 (2004).

- [35] A. Flacco, F. Sylla, M. Veltcheva, M. Carrié, R. Nuter, E. Lefebvre, D. Batani, and V. Malka, Dependence on pulse duration and foil thickness in high-contrast-laser proton acceleration, *Physical Review E* **81**, 036405 (2010).
- [36] P. Neumayer, R. Bock, S. Borneis, E. Brambrink, H. Brand, J. Caird, E. M. Campbell, E. Gaul, S. Goette, C. Haefner, T. Hahn, H. M. Heuck, D. H. H. Hoffmann, D. Javorkova, H. J. Kluge, T. Kuehl, S. Kunzer, T. Merz, E. Onkels, M. D. Perry, D. Reemts, M. Roth, S. Samek, G. Schaumann, F. Schrader, W. Seelig, A. Tauschwitz, R. Thiel, D. Ursescu, P. Wiewior, U. Wittrock, and B. Zielbauer, Status of PHELIX laser and first experiments, *Laser and Particle Beams* **23**, 385 (2005).
- [37] F. Lindau, O. Lundh, A. Persson, P. McKenna, K. Osvay, D. Batani, and C.-G. Wahlström, Laser-accelerated protons with energy-dependent beam direction, *Physical Review Letters* **95**, 175002 (2005).
- [38] D. Batani, R. Jafer, M. Veltcheva, R. Dezulian, O. Lundh, F. Lindau, A. Persson, K. Osvay, C. G. Wahlström, D. C. Carroll, P. McKenna, A. Flacco, and V. Malka, Effects of laser prepulses on laser-induced proton generation, *New Journal of Physics* **12**, 045018 (2010).
- [39] K. Zeil, S. D. Kraft, S. Bock, M. Bussmann, T. E. Cowan, T. Kluge, J. Metzkes, T. Richter, R. Sauerbrey, and U. Schramm, The scaling of proton energies in ultrashort pulse laser plasma acceleration, *New Journal of Physics* **12**, 045015 (2010).
- [40] W. P. Wang, B. F. Shen, H. Zhang, Y. Xu, Y. Y. Li, X. M. Lu, C. Wang, Y. Q. Liu, J. X. Lu, Y. Shi, Y. X. Leng, X. Y. Liang, R. X. Li, N. Y. Wang, and Z. Z. Xu, Effects of nanosecond-scale prepulse on generation of high-energy protons in target normal sheath acceleration, *Applied Physics Letters* **102**, 224101 (2013).
- [41] K. Burdonov, A. Fazzini, V. Lelasseux, J. Albrecht, P. Antici, Y. Ayoul, A. Beluze, D. Cavanna, T. Ceccotti, M. Chabanis, *et al.*, Characterization and performance of the Apollon Short-Focal-Area facility following its commissioning at 1 PW level, *Matter and Radiation at Extremes* **6**, 064402 (2021).
- [42] P. Bolton, M. Borghesi, C. Brenner, D. Carroll, C. De Martinis, F. Fiorini, A. Flacco, V. Floquet, J. Fuchs, P. Gallegos, D. Giove, J. Green, S. Green, B. Jones, D. Kirby, P. McKenna, D. Neely, F. Nuesslin, R. Prasad, S. Reinhardt, M. Roth, U. Schramm, G. Scott, S. Ter-Avetisyan, M. Tolley, G. Turchetti, and J. Wilkens, Instrumentation for diagnostics and control of laser-accelerated proton (ion) beams, *Physica Medica* **30**, 255–270 (2014).
- [43] J. Fuchs, P. Antici, E. d’Humières, E. Lefebvre, M. Borghesi, E. Brambrink, C. A. Cecchetti, M. Kaluza, V. Malka, M. Manclossi, S. Meyroneinc, P. Mora, J. Schreiber, T. Toncian, H. Pépin, and P. Audebert, Laser-driven proton scaling laws and new paths towards energy increase, *Nature Physics* **2**, 48–54 (2005).
- [44] Y. Sentoku, T. E. Cowan, A. Kemp, and H. Ruhl, High energy proton acceleration in interaction of short laser pulse with dense plasma target, *Physics of Plasmas* **10**, 2009 (2003).
- [45] E. Lefebvre, N. Cochet, S. Fritzler, V. Malka, M.-M. Aléonard, J.-F. Chemin, S. Darbon, L. Disdier, J. Faure, A. Fedotoff, *et al.*, Electron and photon production from relativistic laser–plasma interactions, *Nuclear Fusion* **43**, 629 (2003).
- [46] S. Bardy, B. Aubert, T. Bergara, L. Berthe, P. Combis, D. Hébert, E. Lescoute, Y. Rouchausse, and L. Videau, Development of a numerical code for laser-induced shock waves applications, *Optics Laser Technology* **124**, 105983 (2020).
- [47] K. S. Holian, A new equation of state for aluminum, *Journal of Applied Physics* **59**, 149 (1986).
- [48] S. P. Lyon and J. D. Johnson, *Sesame: The Los Alamos National Laboratory equation of state database*, Tech. Rep. LANL LA-UR-92-3407 (Los Alamos National Laboratory, 1992).
- [49] Y. B. Zel’dovich and Y. P. Raizer, *Physics of shock waves and high-temperature hydrodynamic phenomena* (New York, 1967).
- [50] See Supplemental Material for additional experimental data.
- [51] J. Psikal, Effect of the rising edge of ultrashort laser pulse on target normal sheath acceleration of ions, *Plasma Physics and Controlled Fusion* **66**, 045007 (2024).
- [52] S. Monchocé, S. Kahaly, A. Leblanc, L. Videau, P. Combis, F. Réau, D. Garzella, P. D’Oliveira, P. Martin, and F. Quéré, Optically Controlled Solid-Density Transient Plasma Gratings, *Phys. Rev. Lett.* **112**, 145008 (2014).

Supplementary Material: A “lighthouse” laser-driven staged proton accelerator allowing for ultrafast angular and spectral control

V. Horny^{1,2,3,4,*} K. Burdonov^{1,5} A. Fazzini¹ V. Lelasseux^{1,4} P. Antici⁶
 S.N. Chen⁴ A. Ciardi⁵ X. Davoine^{2,3} E. d’Humières⁷ L. Gremillet^{2,3}
 L. Lecherbourg^{2,3} F. Mathieu¹ D. Papadopoulos¹ W. Yao^{1,5} and J. Fuchs^{1,†}

¹LULI - CNRS, CEA, Sorbonne Université, Ecole Polytechnique,
 Institut Polytechnique de Paris - F-91128 Palaiseau cedex, France

²CEA, DAM, DIF, 91297 Arpaçon, France

³Université Paris-Saclay, CEA, LMCE, 91680 Bruyères-le-Châtel, France

⁴ELI NP, “Horia Hulubei” National Institute for Physics and Nuclear Engineering,
 30 Reactorului Street, RO-077125, Bucharest-Magurele, Romania

⁵Sorbonne Université, Observatoire de Paris,
 Université PSL, CNRS, LERMA, F-75005, Paris, France

⁶INRS-EMT, 1650, boulevard Lionel-Boulet, J3X 1S2, Varennes (Québec), Canada

⁷Université de Bordeaux, CNRS, CEA, CELIA (Centre
 Lasers Intenses et Applications), UMR 5107, Talence, France

(Dated: April 18, 2024)

I. HYDRODYNAMICAL SIMULATION

Figure S1 illustrates the longitudinal density profiles (normalized to the critical density n_c) of the expanding electron (blue solid line) and ion (orange solid line) components of the foil target, as extracted at the end of the hydrodynamical simulation ($t = -1$ ps relative to the laser peak). At this point, the critical-density surface ($n_e = n_c$) has shifted approximately 2–3 μm away from the initial target surface (black dashed line), with a local density scale-length $(\partial \ln n_e / \partial x)^{-1} \simeq 2 \mu\text{m}$. The shock initiated within the target bulk appears as a density peak located at $x \simeq 0.4 \mu\text{m}$.

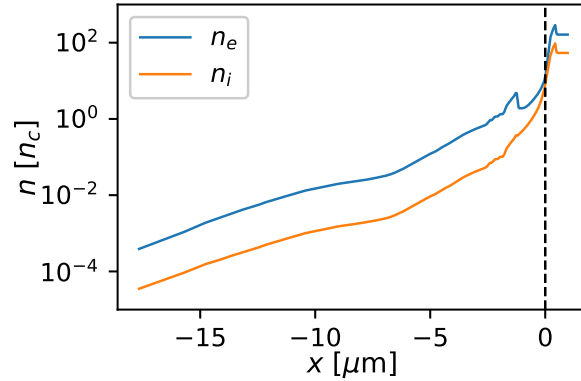


FIG. S1. Longitudinal electron (blue) and ion (orange) density profiles 1 ps before the pulse maximum, as predicted by a 1D ESTHER hydrodynamic simulation using the measured temporal laser profile [1]. The dashed line locates the unperturbed target front surface.

II. NUMERICAL PARAMETERS OF THE PIC SIMULATION

The plasma evolution within the last picosecond before the pulse maximum and the associated ion acceleration are simulated by the particle-in-cell (PIC) method, employing the 2D3V (2D in space, 3D in momentum space) version of the CALDER code [2]. The numerical domain, of dimensions $L_x \times L_y =$

* vojtech.horny@eli-np.ro

† julien.fuchs@polytechnique.edu

$50.93 \times 61.11 \mu\text{m}^2$, is discretized into $10\,000 \times 12\,000$ cells of size $\Delta x = \Delta y = 5.093 \text{ nm}$. The laser pulse is injected from the left-hand side and focused at 45° incidence to a $3 \mu\text{m}$ full-width-at-half-maximum spot located at $(x_f, y_f) = (20, 0) \mu\text{m}$, corresponding to the unperturbed target surface. The temporal laser intensity profile reproduces that plotted in Fig. 1(b) in the main text.

The density profile of the plasma Al ions (n_i) in the longitudinal direction is taken from the hydrodynamic simulation, while it is assumed uniform in the transverse direction. To mitigate spurious numerical heating throughout the ps simulation timescale, the electron and ion temperatures are set to 0.1 eV everywhere while the ion charge state is set to $Z^* = 3$. Accordingly, the electron density profile is initialized to $n_e = Z^* n_i$. This simplification is justified because the intense rising edge of the laser profile will rapidly bring the plasma to a higher ionization state consistent with the experimental reality. In addition, a $2\Delta x$ thick layer of hydrogen atoms of density $n_p = 60 n_c$ is attached to the target backside, modeling the surface contaminants from which protons are accelerated. The Al, H and electron species are initially represented by 4, 1000 and 4 macroparticles per cell, respectively. Elastic collisions between all plasma species and electron impact ionization [3] are described along with field-induced ionization [4]. To further reduce numerical heating, fourth-order weight factors and the Godfrey-Vay [5] and Friedman [6] filtering schemes are used. Moreover, a two-pass compensated binomial filter is applied to smooth the current density.

III. DISCUSSION OF THE 2D SIMULATION GEOMETRY ACCURACY

Our simulations replicate the physics behind the observed proton beam bending, yet the energy of the fastest protons from $1\text{--}5 \mu\text{m}$ thick targets lies in the $\sim 50\text{--}60 \text{ MeV}$ range [see Fig. 4(b) in the main text], about twice that observed in the experiment. This difference can be attributed to the idealized (Gaussian) transverse envelope of the laser beam and, above all, to the simplified (2D) simulation geometry, which is known to overestimate the efficiency of TNSA [7, 8]. This discrepancy likely accounts for the underestimated proton deviation seen in the simulation, as the longitudinal acceleration field is overestimated. Unfortunately, a full 3D simulation with the required resolution and duration is still beyond our computational reach.

-
- [1] K. Burdonov, A. Fazzini, V. Lelasseux, J. Albrecht, P. Antici, Y. Ayoul, A. Beluze, D. Cavanna, T. Ceccotti, M. Chabanis, *et al.*, *Matter and Radiation at Extremes* **6**, 064402 (2021).
 - [2] E. Lefebvre, N. Cochet, S. Fritzler, V. Malka, M.-M. Aléonard, J.-F. Chemin, S. Darbon, L. Disdier, J. Faure, A. Fedotoff, *et al.*, *Nuclear Fusion* **43**, 629 (2003).
 - [3] F. Pérez, L. Gremillet, A. Decoster, M. Drouin, and E. Lefebvre, *Physics of Plasmas* **19**, 083104 (2012).
 - [4] R. Nuter, L. Gremillet, E. Lefebvre, A. Lévy, T. Ceccotti, and P. Martin, *Physics of Plasmas* **18**, 033107 (2011).
 - [5] B. B. Godfrey and J.-L. Vay, *Journal of Computational Physics* **267**, 1 (2014).
 - [6] A. D. Greenwood, K. L. Cartwright, J. W. Luginsland, and E. A. Baca, *Journal of Computational Physics* **201**, 665 (2004).
 - [7] A. Sgattoni, P. Londrillo, A. Macchi, and M. Passoni, *Physical Review E* **85**, 036405 (2012).
 - [8] Y. Takagi, N. Iwata, E. d’Humières, and Y. Sentoku, *Physical Review Research* **3**, 043140 (2021).